Macromolecules

pubs.acs.org/Macromolecules

Article

Time–Temperature Superposition of Polybutadiene Vitrimers

Ralm G. Ricarte,* Sachin Shanbhag,* Dana Ezzeddine, Daniel Barzycki, and Kevin Fay

Cite This: https://doi.org/10.1021/acs.macromol.3c00883

Read Online

ACCESS | Metrics & More | Article Recommendations | Supporting Information

ABSTRACT: A vitrimer has covalent cross-links that preserve network connectivity but permit topology fluctuations through dynamic exchange reactions. In this work, we investigate the linear rheology of polybutadiene (PB) vitrimers bearing cross-links that exchange via dioxaborolane metathesis. PB vitrimers are cross-linked in solution using photoinitiated thiol-ene click chemistry. As the targeted cross-link density is increased, both the insoluble fraction and glass-transition temperature increase. Linear viscoelasticity is studied using a combination of small-amplitude oscillatory shear (SAOS), creep, and stress relaxation measurements. In SAOS, the elastic modulus is approximately constant while the viscous modulus increases as angular frequency decreases. In creep, the compliance displays power law behavior that persists for at least 8 h. In stress relaxation, the modulus transitions from a rubbery plateau into a power law regime. Both SAOS and creep data are visually superposed into master curves using horizontal shift factors that exhibit Arrhenius behavior. However, the application of these determined shift factors to stress relaxation curves fails to align the data into a single master curve. SAOS shift factors (a_{SAOS}) collapse the short-time relaxation data, and their activation energy (E_a^{SAOS}) matches the effective Williams–Landel–Ferry activation energy for PB homopolymer, indicating that the short-time dynamics correspond to network strand segment relaxations. Creep shift factors (a_{creep}) collapse the long-time relaxation data, and their activation energy (E_a^{creep}) is significantly larger than the energies predicted by established theoretical models for transient networks. We speculate that the discrepancy between experiment and theory is due to the temperature dependence of the cross-linker mobility within the vitrimer matrix, which is not fully captured by established theoretical models.

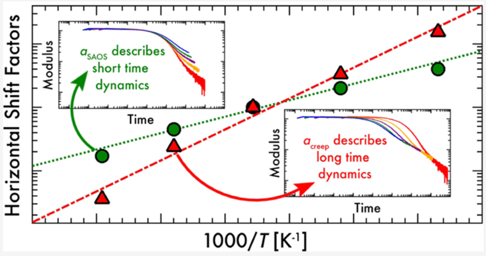

■ INTRODUCTION

Dynamic covalent polymer networks—also known as transient networks, reversible networks, or covalent adaptable networks—contain cross-links between chains that exchange through a chemical reaction.[1−5] From a theoretical perspective, such networks were first modeled by Green and Tobolsky to rationalize the stress relaxation behavior of vulcanized rubbers. In their theory, stress decays exponentially and follows an Arrhenius-like relationship with temperature.[6] Flory, and later Fricker, considered similar systems in which cross-links within a network ruptured and reformed simultaneously, thereby preserving network connectivity but enabling network topology fluctuations. Based on both intuitive and mathematically rigorous arguments, they predicted that at long time, stress relaxation exhibits a power law decay governed by the lifetime of a cross-link (τ_{XL}).[7−9] Baxandall and Leibler et al. separately developed reversible network theories that accounted for the primitive Rouse and reptation relaxations of network strands. According to these sticky Rouse and sticky reptation models, three distinct time regimes occur in stress relaxation: (I) an initial decay representative of Rouse motions, (II) a rubbery plateau whose modulus is proportional to the sum of the cross-link and entanglement densities, and (III) a terminal relaxation directly controlled by τ_{XL}.[10−12] In this work, we study the different time regimes during the relaxation of polybutadiene vitrimers, a class of dynamic covalent polymer networks that engage in associative exchange reactions.

Vitrimer cross-links exchange through an addition/elimination pathway, i.e., a new covalent linkage between two chains is formed before an existing bond is fragmented. As a consequence, the network maintains connectivity and constant cross-link density, thereby preventing the dissolution of polymer in a good solvent at all temperatures below backbone degradation conditions. At the same time, however, cross-link exchange enables the network topology to fluctuate and the material to flow.[2−5] This combination of solvent resistance and processability makes vitrimers not only appealing for improving plastic sustainability and high-performance applications,[13−33] but also as a platform for investigating how dynamic cross-links impact the physics of the underlying polymer chains.

In particular, understanding vitrimer rheology has garnered significant interest, as their viscoelasticity regulates the efficiency of their processing and recycling. In the seminal

Received: May 6, 2023
Revised: July 31, 2023

Scheme 1. Synthetic Scheme for Polybutadiene (PB) Vitrimers

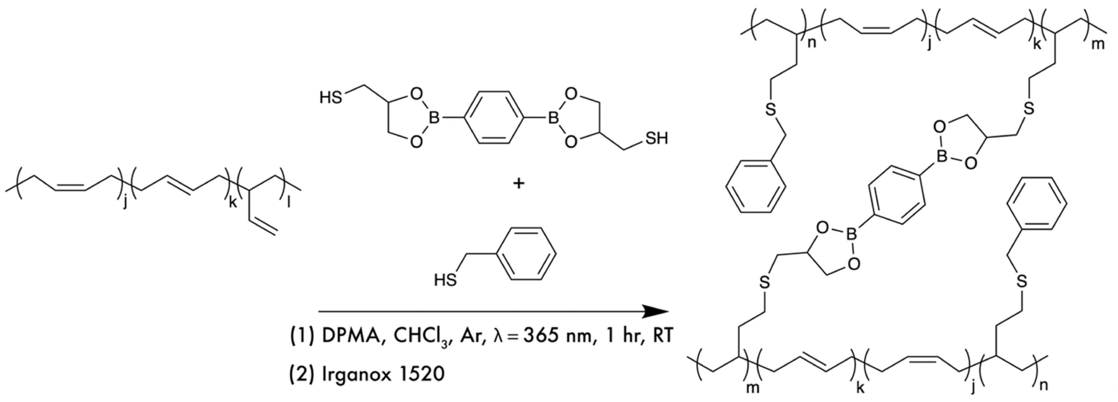

works of Montarnal, Tournilhac, Leibler, and co-workers, epoxy vitrimers whose cross-links exchanged via a metal-catalyzed transesterification had stress relaxation behavior that could be described by a monomodal exponential decay. The relaxation rate obeyed an Arrhenius relationship with temperature, with the apparent activation energy from rheology (E_a^{rh}) being comparable to the activation energy for transesterification in small-molecule analogues of the epoxy network (E_a^{sm}).[34−36] As the vitrimer concept was translated to different backbone and cross-link chemistries, however, deviations from these simple trends were seen. E_a^{rh} values are usually much larger than the E_a^{sm}.[15,20,37−40] Broad nonexponential decays are commonly observed in stress relaxation.[41−50] The temperature dependence over a wide range cannot be described by a single activation energy.[48,51−54]

Responding to these observations, experimental, computational, and theoretical efforts over the past 5 years have focused on illuminating the relationship between vitrimer viscoelasticity and temperature. Generally, the relaxation rate expresses two different temperature regimes, where the estimated activation energy of the low-temperature regime is less than that of the high-temperature regime.[48,49,51,53,55−57] In 2021, Ricarte and Shanbhag used a generalized form of the sticky Rouse model to evaluate the role of backbone and cross-link chemistry on vitrimer viscoelasticity. At temperatures well above the glass transition, they observed that the short-time dynamics represented monomer friction. The activation energy associated with this time regime corresponded to an effective activation energy that could be calculated using the Williams−Landel−Ferry (WLF) parameters for the vitrimer backbone (E_a^{WLF}). Conversely, the intermediate and terminal dynamics portrayed a combination of network strand relaxation and cross-link exchange. The resulting activation energy of this long-time regime (E_a^{sticky}) was estimated by the simple formula

$$E_a^{sticky} = E_a^{WLF} + E_a^{sm} \tag{1}$$

Due to the different activation energies of each regime, time−temperature superposition of the entire relaxation spectrum could not be achieved. However, the short- and long-time relaxation regimes were superposed using different sets of horizontal shift factors.[58]

Using our previous sticky Rouse modeling as a guide, in this work, we investigate the thermorheological behavior of polybutadiene (PB) vitrimers bearing dioxaborolane cross-links (Scheme 1). The combination of a flexible polymer backbone and relatively slow cross-link exchange kinetics allows us to separate the short- and long-time relaxation dynamics. Furthermore, the E_a^{sm} for small-molecule dioxaborolane metathesis has already been measured,[15] facilitating comparison of the activation energies from rheology. We probe the linear viscoelasticity of PB vitrimers with varying cross-link density using a combination of small-amplitude oscillatory shear (SAOS), creep, and stress relaxation measurements. At temperatures over 100 °C above the glass transition, PB vitrimers achieve power law behavior that persists for at least 8 h. SAOS and creep data are collapsed using different sets of horizontal shift factors (a_{SAOS} and a_{creep}) that each follows Arrhenius temperature dependences. The activation energies associated with a_{SAOS} match the expected E_a^{WLF} values for PB homopolymer, suggesting that the short-time dynamics correspond to PB segment relaxations. In contrast, the activation energies associated with a_{creep} are larger than the E_a^{sticky} values expected from eq 1, especially at higher cross-link densities. We speculate that this discrepancy stems from the temperature dependence of the cross-link mobility within the PB matrix (σ). Attempts to describe the σ temperature dependence using established microscopic models are discussed.

■ MATERIALS AND METHODS

Materials. Polybutadiene (M_N = 6800 g/mol, $Đ$ = 1.41, 1,2-addition = 12 mol %), benzyl mercaptan, 1,4-benzenedimethanethiol, 2,2-dimethoxy-2-phenylacetophenone, 1,2-octanediol, chloroform, and tetrahydrofuran were obtained from Sigma-Aldrich. Benzene-1,4-diboronic acid was obtained from Apollo Scientific. 2-Methyl-4,6-bis[(*n*-octylthio)methyl]phenol (Irganox 1520) was obtained from TCI Chemicals. Magnesium sulfate was obtained from VWR.

Size Exclusion Chromatography (SEC) of Precursor Polybutadiene (PB). SEC of the precursor PB was performed using an Agilent-Wyatt combination triple-detection SEC instrument equipped with three successive Agilent PL-gel Mixed C columns (25 °C THF mobile phase). The instrument also featured an Agilent 1260 infinity series pump, degasser, autosampler, and thermostatted column chamber. The triple-detection unit consisted of a MiniDawn TREOS 3-angle light scattering detector, Optilab TrEX refractive index detector, and a Viscostart II differential viscometer. For the determination of the absolute molar masses, a refractive index increment of 0.134 was used.[59]

Synthesis of 2,2′-(1,4-Phenylene)-bis[4-thioethyl-1,3,2-dioxaborolane] (Dioxaborolane Cross-Linker). The synthesis of the dioxaborolane cross-linker was conducted based on the scheme reported in Breuillac et al.[60] Benzene-1,4-diboronic acid (10 g), 3-mercapto-1,2-propanediol (13.38 g), and tetrahydrofuran (100 mL) were combined in a round-bottom flask and stirred for 5 min. Magnesium sulfate (16.66 g) was added, and the mixture was stirred at room temperature for 48 h, filtered, and concentrated under reduced pressure. The remaining precipitate was dried under reduced pressure at 100 °C for 18 h to yield 16.9 g of a white powder (81% yield). Figure S5 shows the ^{1}H NMR spectrum (600 MHz, $CDCl_3$): δ 7.81 (s, 4H), 4.74 (q, J = 6.2 Hz, 2H), 4.50 (m, 2H), 4.17 (m, 2H), 2.81 (m, 4H), 1.48 (t, J = 8.6 Hz, 2H). Figure S6 is the ^{13}C NMR spectrum (600 MHz, $CDCl_3$): δ 134.3, 77.7, 70.0, 29.8. The carbon adjacent to the boron was not detected.

PB Vitrimer Synthesis. PB vitrimers were prepared using photoinitiated thiol-ene click chemistry. The polymer backbone was functionalized using a mixture of dioxaborolane cross-linker and benzyl mercaptan. Varying the ratio of dioxaborolane cross-linker to benzyl mercaptan allowed the cross-link density to be tuned while maintaining a constant amount of sulfide and aromatic groups within the sample. This approach also permitted the feed ratio of thiol groups of the cross-linker/benzyl mercaptan and 1,2-adducts of PB to be stoichiometric for each sample reaction mixture, minimizing the occurrence of parasitic cyclization reactions.[61] Table 1 lists the sample names and targeted number of dioxaborolane cross-links and benzyl mercaptan groups. Samples are named as PB-v-N_{XL}, where N_{XL} is the targeted number of dioxaborolane cross-links per PB chain.

Table 1. PB Vitrimer Targeted Number of Cross-Links (N_{XL}) and Benzyl Mercaptan Groups (N_{BM}) Per PB Chain[a]

sample ID	N_{XL}	N_{BM}
PB-v-1	1	14
PB-v-4	4	11
PB-v-8	8	7
PB-v-15	15	0

[a] For all samples, the targeted number of sulfides per PB chain $N_{sulfide} = N_{XL} + N_{BM} = 15$.

Scheme 1 outlines the synthetic procedure for PB vitrimers. To prepare PB-v-4, polybutadiene (1.00 g, 2.2 mmol of vinyl groups), dioxaborolane cross-linker (0.09516 g, 0.275 mmol), benzyl mercaptan (0.2049 g, 1.65 g), 2,2-dimethoxy-2-phenylacetophenone (0.0575 g, 0.22 mmol), and dry chloroform (4.8 mL) were mixed in a scintillation vial, transferred into a 10 mL cylindrical single-neck Schlenk flask, and degassed through three freeze−pump−thaw cycles. Cross-linking was performed by exposing the reaction mixture to UV light (MelodySusie Model DR-301Z, λ = 365 nm, flux = 800 μW/cm^2) for 1 h. After UV exposure, the resulting gel was doped with 0.1 mL of a solution containing 0.002 g of Irganox 1520 dissolved in dry chloroform and then stored in the dark at ambient temperature for 24 h. The gel was then transferred to a scintillation vial and dried under reduced pressure at 75 °C for 18 h to yield 1.13 g of a translucent solid.

Thermal Characterization. Differential scanning calorimetry was performed using a TA Instruments DSC Q2000. 4−5 mg of sample was placed inside an aluminum pan with a standard lid. Under a nitrogen gas flow of 50 mL/min, PB vitrimer samples were first cooled from 0 to −80 °C, heated to 180 °C, cooled to −80 °C, and finally reheated to 180 °C. All heating and cooling rates had a magnitude of 10 °C/min. The glass-transition temperature (T_g) was measured from the inflection point in the second heating trace. All samples were examined by DSC in triplicate.

Insoluble Fraction Measurement. The insoluble content of PB vitrimer samples was quantified using the method of Röttger et al.[15] 0.1 g of sample was placed inside a stainless steel fine wire cage and submerged in 40 g of dried chloroform. After 24 h, the cage was removed from the solvent and dried under reduced pressure at 75 °C for at least 18 h. The mass of the remaining insoluble portion of the vitrimer was measured to determine the insoluble fraction. The sample remaining in the cage was then resubmerged in a chloroform solution containing an excess of 1,2-octanediol. The addition of the diol caused each of the vitrimer samples to fully dissolve, confirming the absence of nondynamic static cross-links in the PB vitrimer networks.

Rheology Measurements. Linear viscoelasticity of PB vitrimers was evaluated using an Anton Paar MCR 302e rotational rheometer equipped with parallel plate geometry. The upper geometry was an 8 mm aluminum disposable plate, while the lower geometry was a 25 mm stainless steel plate with Peltier temperature control. To minimize sample slip, both upper and lower plates had profiled surfaces. To minimize thermal degradation, the plate geometry was encased in a hood under a 200 L/h nitrogen flow. The geometry achieved a temperature control accuracy of ±0.1 °C. During measurements, a normal force between 0.1 and 1 N was applied to maintain contact between the sample and upper plate. PB vitrimer samples were molded into disk shapes (8 mm diameter and 1.5 mm thickness) using stainless steel frames, which were subjected to an applied load of 3 tons at 150 °C for 8 min.

Strain amplitude sweeps, small-amplitude oscillatory shear (SAOS), stress relaxation, and creep compliance and recovery measurements were conducted. From the strain amplitude sweeps (Figure S12), a linear viscoelastic regime was identified at temperatures of 100 and 180 °C. For SAOS and stress relaxation, measurements on fresh samples at all temperatures were performed at an imposed strain value that was within both the linear viscoelastic regimes identified at 100 and 180 °C (see Table S1). To improve the reproducibility of results, samples were subjected to a preconditioning routine prior to SAOS, stress relaxation, and creep measurements. The preconditioning routine is detailed in the Supporting Information (see Figure S13). SAOS measurements were run at angular frequencies (ω) ranging from 100 to 0.01 rad/s. Stress relaxation measurements were run for 8 h. Creep compliance and recovery measurements were run for 8 and 2 h, respectively.

Time−temperature superposition was performed on SAOS, creep compliance, and stress relaxation data using a reference temperature T_R = 120 °C. Vertical shift factors for SAOS (b_{SAOS}) were calculated by

$$b_{SAOS}(T) = \frac{G'_p(T_R)}{G'_p(T)} \tag{2}$$

where $G'_p(T)$ and $G'_p(T_R)$ are the magnitudes of the elastic modulus plateau at temperatures T and T_R, respectively. After applying b_{SAOS}, horizontal shift factors for SAOS measurements (a_{SAOS}) were determined by manually superposing the tan δ data. Vertical shift factors for creep and stress relaxation measurements (b_{creep} and b_{stress}) were determined by

$$b_{stress}(T) = \frac{G_p(T_R)}{G_p(T)} \tag{3}$$

$$b_{creep}(T) = \frac{J_p(T)}{J_p(T_R)} \tag{4}$$

where $G_p(T)$ and $G_p(T_R)$ are the stress relaxation plateau moduli at T and T_R, while $J_p(T)$ and $J_p(T_R)$ are the instantaneous compliances at T and T_R, respectively.[62] Plateau moduli from stress relaxation and instantaneous compliances from creep were calculated by averaging the data between 0.1 and 10 s. After applying b_{creep}, horizontal shift factors for creep measurements (a_{creep}) were determined by manually superposing the compliance data.

Portions of PB vitrimer samples used for rheology were subject to extraction in chloroform in the presence of excess 1,2-octanediol. All samples completely dissolved, suggesting that the material did not form a static cross-linked network during the rheological measurements.

■ RESULTS

PB Vitrimer Characterization. PB vitrimers bearing dioxaborolane cross-links were prepared using photoinitiated thiol-ene click chemistry. The cross-links engage in a dioxaborolane metathesis exchange reaction, which has an

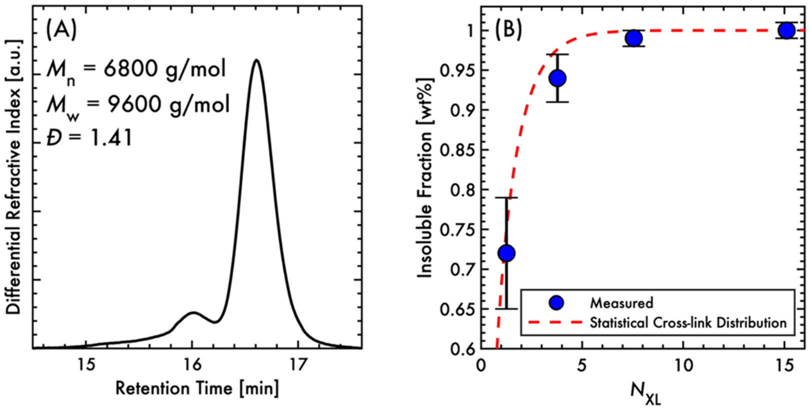

Figure 1. (A) Precursor PB SEC trace. (B) PB vitrimer-insoluble fraction versus targeted number of cross-links per PB chain (N_{XL}). Error bars represent the standard deviation of triplicate measurements.

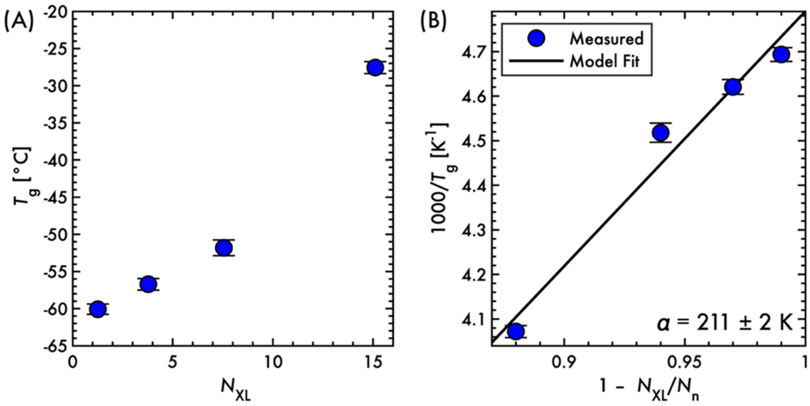

Figure 2. (A) Glass-transition temperature T_g versus N_{XL}. Error bars represent the standard deviation of triplicate measurements. (B) Equation 5 fit to T_g data. Error bars represent propagated error.

activation energy E_a^{sm} = 15.1 kJ/mol. These cross-links are able to exchange without the need of an external catalyst.[3,15] The synthesis and rheology of a static cross-link PB thermoset control sample are described in the Supporting Information.

Table 1 details the targeted number of dioxaborolane cross-links and pendant benzyl mercaptan groups per PB chain (N_{XL} and N_{BM}, respectively) of the vitrimer samples. While both N_{XL} and N_{BM} are varied, their sum—corresponding to the targeted number of sulfide bonds per PB chain (N_S)—is kept constant. The samples featured in this work are labeled as PB-*v*-N_{XL}. Values of N_{XL} ranging from 1 to 15 were targeted. The presence of the dioxaborolane cross-linker and benzyl mercaptan on the PB backbone was confirmed using attenuated total reflectance infrared spectroscopy (ATR-IR). Figures S7 and S8 depict the ATR-IR spectra for each of the PB vitrimer samples. Peak deconvolution of the ATR-IR spectra is described in the Supporting Information (see Figure S30A). Figures S9 and S10 detail their thermal characterization. Figure S11 illustrates PB vitrimer small-angle X-ray scattering patterns from synchrotron and lab-scale X-ray sources.

Figure 1A illustrates the SEC trace of the precursor PB. The peak at 16 min is attributed to the presence of branched chains. Additional characterization of the precursor PB is featured in the Supporting Information (Figures S1−S4).

Figure 1B depicts the insoluble fraction of the PB vitrimers as a function of N_{XL}. The measured insoluble fractions, which increase as N_{XL} increases, are compared to the expected values. The dashed red curve is the estimated weight fraction of chains bearing at least 1 dioxaborolane cross-link, as calculated using eq S3. This line essentially represents the maximum possible insoluble fraction for a system with statistically distributed nondynamic cross-links and the same molar mass distribution as the precursor PB. The measured insoluble fractions match this limit. Along with the featureless scattering patterns observed by SAXS (Figure S11), the agreement between the measured and expected insoluble fractions suggest that the PB vitrimers are not macro- or microphase-separated.

Figure 2A plots the glass-transition temperature (T_g) versus N_{XL}. During differential scanning calorimetry measurements, only a single T_g is observed between −80 and 180 °C (Figure S10). The measured T_g, which increases as N_{XL} increases, can be described using

$$\frac{1}{T_g} = \frac{1}{\alpha}\left(1 - \frac{N_{XL}}{N_n}\right) \tag{5}$$

where $\alpha = 211 \pm 2$ K is an empirical constant determined by using a linear regression. Figure 2B fits eq 5 to the measured T_g values.

Linear Viscoelasticity. Figure S31 focuses on isothermal SAOS measurements for each PB vitrimer sample (see the Supporting Information for experimental details). Over a period of 8 h at 180 °C, each sample exhibits a slight increase in the elastic modulus (G') that eventually reaches a plateau value at later times. The viscous modulus (G'') is essentially

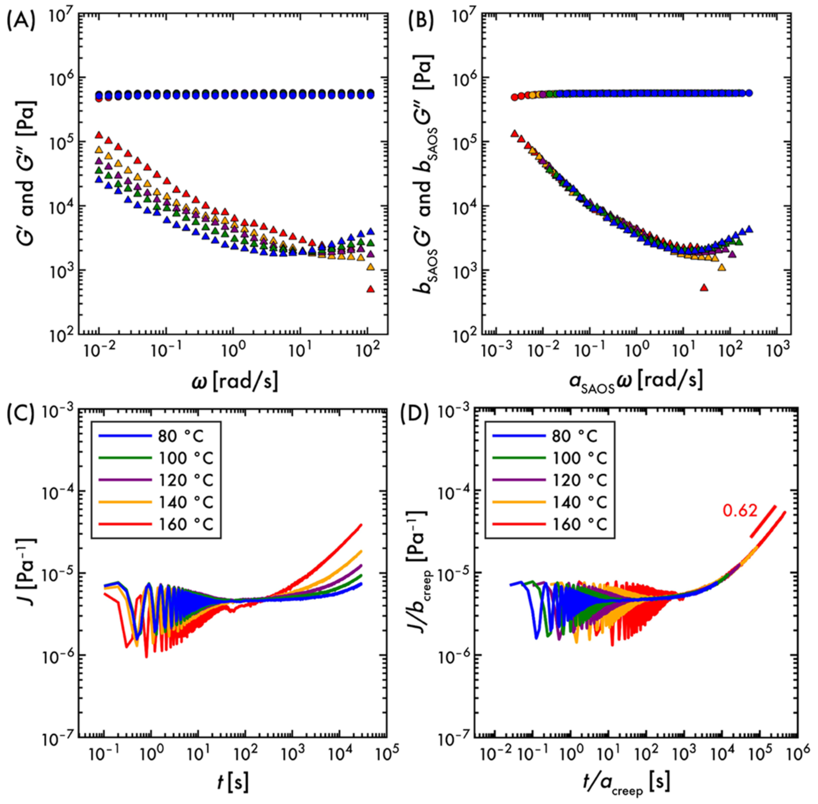

Figure 3. Linear viscoelastic measurements of PB-*v*-4. (A) SAOS as measured and (B) with a_{SAOS} horizontal shift factors applied. (C) Creep as measured and (D) with a_{creep} horizontal shift factors applied. The reference temperature for both a_{SAOS} and a_{creep} is 120 °C.

constant within experimental error. These data suggest that PB vitrimers are relatively stable within the conditions of the rheological measurements performed in this study.

Figures 3A, S14A, S15A, and S16A depict SAOS measurements. For all samples, G' is approximately constant over the range of angular frequencies (ω) from 0.01 to 100 rad/s. The magnitude of G' increases with N_{XL} (Figure S21A). In contrast, G'' increases as ω decreases. The magnitude of the G'' rise increases as temperature increases. tan δ curves, featured in Figure S17, depict similar trends.

Figures 3C, S14C, S15C, and S16C detail creep measurements. Prior to 100 s, the creep compliance (J) exhibits a dampening sinusoidal response, typical of elastic materials.[63,64] After 100 s, J increases and adopts a power law relationship with time. J rises more significantly as the temperature is increased. The power law scaling exponent for J, however, is much lower than the characteristic steady-state flow scaling of 1, even after a period of 24 h (Figure S26). Similarly, the creep recovery compliance (J_{rec}) increases over time but does not reach a plateau over a period of 2 h (Figure S19). The magnitude of J_{rec} increases as temperature increases and N_{XL} decreases.

Figure 3B,D shows SAOS and creep master curves for PB-*v*-4. Master curves for the other samples are listed in the Supporting Information (see Figures S14–S16 and S18). The superposition of the data was performed by applying both vertical and horizontal shift factors. The horizontal shift factors for SAOS and creep are labeled as a_{SAOS} and a_{creep}, respectively. For SAOS, G' and G'' data below $a_{\mathrm{SAOS}}\,\omega = 10$ rad/s collapse into a single curve. Likewise, the J data after $t/a_{\mathrm{creep}} = 10^3$ s superpose into a single curve. Vertical shift factors are plotted in Figure S22.

Figures 4 and S20 plot a_{SAOS} and a_{creep} versus inverse temperature. Although both a_{SAOS} and a_{creep} show an approximate Arrhenius dependence, a_{creep} has a stronger temperature sensitivity. Activation energies $E_{\mathrm{a}}^{\mathrm{SAOS}}$ and $E_{\mathrm{a}}^{\mathrm{creep}}$ are calculated by fitting the following equations to the horizontal shift factors:

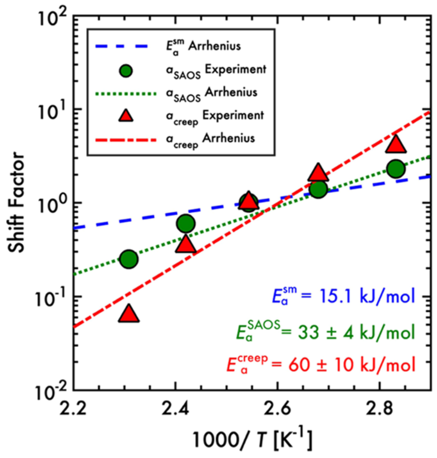

Figure 4. Arrhenius fits of a_{SAOS} and a_{creep} horizontal shift factors for PB-*v*-4. The reference temperature for both a_{SAOS} and a_{creep} is 393.15 K.

$$\ln(a_{\mathrm{SAOS}}) = \frac{E_{\mathrm{a}}^{\mathrm{SAOS}}}{R}\left(\frac{1}{T} - \frac{1}{T_{\mathrm{R}}}\right) + \text{intercept} \tag{6}$$

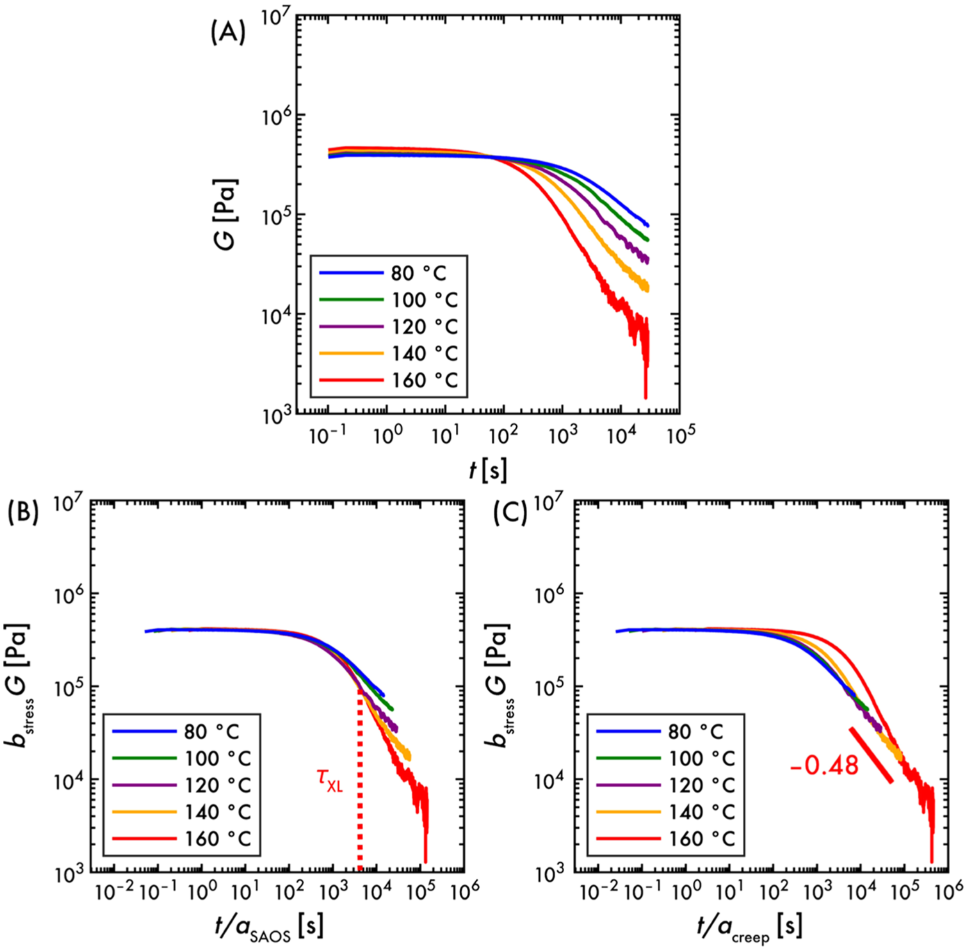

Figure 5. Stress relaxation of PB-v-4 (A) as measured, (B) with a_{SAOS}, and (C) a_{creep} horizontal shift factors applied. In (B), the dashed line represents cross-link lifetime (τ_{XL}) estimated from the Prony series analysis. The reference temperature for both a_{SAOS} and a_{creep} is 120 °C.

$$\ln(a_{\text{creep}}) = \frac{E_a^{\text{creep}}}{R}\left(\frac{1}{T} - \frac{1}{T_R}\right) + \text{intercept} \qquad (7)$$

where T is the temperature, T_R is the reference temperature of 393.15 K, and R is the gas constant. For all samples, $E_a^{\text{creep}} > E_a^{\text{SAOS}} > E_a^{\text{sm}} = 15.1$ kJ/mol.[15] A double Arrhenius analysis was also performed by estimating separate activation energies for temperature ranges of 80−140 and 140−160 °C (Figure S34). Figure S35 depicts the estimated E_a^{SAOS} and E_a^{creep} values from the double Arrhenius analysis. In all cases, $E_a^{\text{creep}} > E_a^{\text{SAOS}} > E_a^{\text{sm}}$.

Figures 5 and S23−S25 illustrate stress relaxation measurements. At early times, the stress relaxation modulus (G) sits on a plateau. The magnitude of this plateau modulus increases with N_{XL} (Figure S21). After ≈ 100 s, G exhibits a relaxation whose rate increases with temperature. Eventually, G displays apparent power law behavior at longer times. Although the low signal-to-noise ratio of the long-time data inhibits the determination of horizontal shift factors from stress relaxation experiments, the application of a_{SAOS} and a_{creep} shift factors demonstrates that the G data do not obey time−temperature superposition over the entire time range. Application of a_{SAOS} causes G to overlap at $\frac{t}{a_{\text{SAOS}}} \lesssim 10^3$ s. Application of a_{creep} causes the apparent power law portion of the G curves to superpose. For PB-v-1 and PB-v-4, power law exponents of approximately −1/2 are identified. For PB-v-8 and PB-v-15, the low signal-to-noise ratio of the 160 °C data prevents precise determination of a power law scaling.

The measured plateau moduli from small-amplitude oscillatory shear (SAOS) and stress relaxation measurements are compared to the Affine and Phantom Network rubber elasticity theories (Figure S21A). Most of the samples are consistent with the Phantom Network prediction except for PB-v-15, which is lower than the targeted value (Figure S21B). Using the Phantom Network theory, N_{XL} values for each sample are estimated. The ATR-IR deconvolution and T_g data are replotted using the Phantom Network N_{XL} values (Figures S30B and S32).

Activation Energies. Figure 6 plots E_a^{SAOS} and E_a^{creep} versus T_g. The E_a^{SAOS} data are compared to the following E_a^{WLF} model:

$$E_a^{\text{WLF}} = \frac{2.303 C_1 C_2 T_R^2}{(C_2 + T_R - T_g - 55\ \text{K})^2} \qquad (8)$$

where T_g is the glass-transition temperature measured from DSC, $T_R = 393.15$ K is the reference temperature, and C_1 and C_2 are the WLF parameters for PB homopolymer (see the Supporting Information for derivation). Not only are the measured E_a^{SAOS} consistent with the rheological activation energy of the precursor PB (Figure S4C), but they also quantitatively match the expected E_a^{WLF} values estimated using eq 8. E_a^{creep} data are compared to the overall activation energy predicted by the sticky Rouse and sticky reptation theories

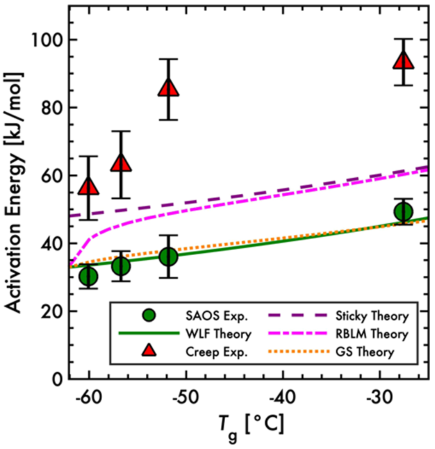

Figure 6. Comparison of measured activation energies from SAOS and creep versus WLF, sticky Rouse and sticky reptation (Sticky), renormalized bond lifetime (RBLM), and Ghosh−Schweizer (GS) models. The reference temperature for all activation energies is 393.15 K. Error bars represent the standard error from the Arrhenius fits.

(E_a^{sticky}, eq 1). At low N_{XL} and T_g, E_a^{creep} is comparable to E_a^{sticky}. As N_{XL} and T_g increase, however, the discrepancy between E_a^{creep} and E_a^{sticky} grows larger.

Summary of Linear Viscoelasticity Results. SAOS, creep, and stress relaxation measurements were performed on PB vitrimers with varying cross-link density. Both SAOS and creep data exhibit approximate Arrhenius relationships with temperature, but the resulting horizontal shift factors have different activation energies. E_a^{SAOS} is consistent with predictions from the WLF theory, while E_a^{creep} grows to be much larger than the predictions from sticky Rouse and sticky reptation theories.

DISCUSSION

PB Vitrimer Cross-Link Density and Morphology. PB vitrimers were prepared in solution by co-functionalizing the precursor polymer with both dioxaborolane cross-linker and benzyl mercaptan. This co-functionalization approach was used to maintain a stoichiometric ratio between the cross-linker/benzyl mercaptan thiols and the PB 1,2-adducts. Without the inclusion of benzyl mercaptan, decreasing the cross-link density would lead to an excess of vinyl groups in the reaction mixture, increasing the occurrence of parasitic cyclization reactions.[61] The consistency between E_a^{SAOS} values of the precursor PB and the PB vitrimers suggests that the presence of benzyl mercaptan has minimal impact on the segmental relaxation of the vitrimer backbone.

In contrast to previously studied polyethylene (PE) vitrimers bearing dioxaborolane cross-links,[81] the PB vitrimers of this study do not exhibit any evidence of macro- or microphase separation. We posit that this difference in morphology results from the synthetic protocol. The PE vitrimers in ref 81 were prepared using a two-step reactive extrusion scheme, in which dioxaborolane maleimide was first radically grafted onto the backbone, and then a bis-dioxaborolane cross-linker was added to form the network. Dioxaborolane maleimide was observed to be immiscible in molten PE. As such, the first step of the reactive extrusion scheme already introduced heterogeneities into the material. Dynamic cross-linking alters the nanostructure, but aggregates were formed once dioxaborolane maleimide was grafted onto the backbone.[81] For the PB vitrimers in the present study, cross-linking is performed in solution. Chloroform is a good solvent for both the PB and dioxaborolane cross-linker. After cross-linking, the resulting gel is transparent. After drying, the resulting vitrimer is translucent. Furthermore, the DSC traces only exhibit a single glass transition. These observations, in conjunction with the featureless SAXS patterns, suggest the PB vitrimers are homogeneous.

Short- and Long-Time Linear Viscoelastic Regimes. In the linear viscoelastic regime, PB vitrimers exhibit relaxations that are not observed for the static cross-link PB thermoset control sample (Scheme S1 and Figure S27). For many vitrimer systems, time−temperature superposition is successful at collapsing viscoelastic data that occur during the initial transition from the rubbery plateau regime to longer time relaxations. In SAOS, for instance, this corresponds to the region surrounding the $G'-G''$ crossover frequency (ω_{cross}). For measurements collected over wide time or frequency ranges, however, the short- and long-time dynamics do not superpose into a single master curve.[39,51,53,54] As evidenced by the different shift factors for SAOS and creep experiments in this study, the thermorheological behavior of PB vitrimers agrees with these trends.

The PB vitrimer $G'$and G'' only capture the dynamic response of the rubbery plateau regime. According to the framework of the sticky Rouse and sticky reptation models, this describes the time period between the Rouse decay of the glassy modes and the first instance of cross-link exchange ($\tau_{XL} = \frac{1}{\omega_{cross}}$).[11] The agreement between the measured E_a^{SAOS} and predicted E_a^{WLF} strongly suggests that the observed upturn in G'' represents segmental motions of the PB network strands. As this behavior occurs at frequencies above ω_{cross}, we propose that subdiffusive segmental motions facilitate cross-link exchange events. This concept is consistent with previous theoretical arguments regarding reactive polymer systems.[65−74]

For the long-time dynamics, the interpretation is much more complex. The beginning of this regime is signaled by τ_{XL} (or, equivalently, ω_{cross}). Although we do not directly capture the $G'-G''$ crossover in our SAOS data, we can roughly approximate it by fitting the stress relaxation modulus to an empirical Prony series, and then using the fitting parameters to extrapolate G' and G'' to lower angular frequencies (see Figure S28). As an example, for PB-ν-4 at 120 °C, we estimate $\tau_{XL} \approx$ 4000 s, which coincides with the time point in which time−temperature superposition begins to fail in the stress relaxation master curve depicted in Figure 5B. The origin of the lengthy power law regime is less clear. For stress relaxation, the sticky Rouse model anticipates an intermediate relaxation regime in which $G \sim t^{1/2}$.[11,12,58,75−79] Hybrid Monte-Carlo molecular dynamics simulations by Perego and Khabaz also detected intermediate regimes of $G \sim t^{1/2}$ in stress relaxation and $J \sim t^{1/2}$ in creep.[53] This intermediate regime is expected to last until a terminal relaxation time (τ_1) is reached. While sticky Rouse theory expects that $\tau_1 \sim \tau_{XL} N_{XL}^2$,[58] we do not observe any indication of terminal relaxation in our rheological measurements, even for PB-ν-1. Moreover, the transient network model of Fricker actually associates terminal relaxation with a $G \sim t^{1/2}$ scaling.[8,9] Without directly observing τ_1, we cannot precisely assign the measured long-time dynamics to a particular relaxation regime.

For the SAOS and creep shift factors in Figures 4 and S20, the data possibly display an inflection point between 140 and

160 °C. The double Arrhenius analysis depicted in Figures S34 and S35 produces different apparent activation energies for the 80−140 and 140−160 °C ranges. For the 80−140 °C range, the activation energies are systematically 5 kJ/mol lower than the values from Figure 6. Yet, the trends for the SAOS and creep curves remain the same. For the 140−160 °C range, the activation energies are larger than the values from Figure 6. Because these values result from a linear regression on two data points, however, we do not ascribe any physical meaning to activation energies estimated from this range. Nevertheless, the creep activation energies are still larger than the SAOS activation energies, which is consistent with the original interpretation of Figure 6.

Thus, the double Arrhenius analysis still produces the same conclusion as before: the short- and long-time dynamics of the PB vitrimers have different temperature dependences.

One possible cause of the inflection point between 140 and 160 °C is the thermal history of the sample. Although the PB vitrimers undergo a preconditioning routine at each temperature, terminal relaxation is not observed for any sample within experimental time scales. As such, the measurements at 160 °C may be affected by unresolved stresses instilled into the vitrimers during sample preparation or loading into the rheometer. Future studies are needed to understand the role of thermal history on vitrimer rheology.

Activation Energy of Long-Time Viscoelastic Regime. For the temperature dependence of the long-time dynamics, the measured E_a^{creep} and predicted E_a^{sticky} diverge as N_{XL} and, consequently, T_g increase. This relationship is similar to the trend Hajj et al. observed for the activation energy of vitrimer networks bearing imine cross-links.[40] We suspect that the discrepancy between E_a^{creep} and E_a^{sticky} potentially arises from an assumption in our previous work.[58] There, we described τ_{XL} using

$$\tau_{\text{XL}} = \sigma\tau_0 \exp\left(\frac{E_a^{\text{sm}}}{RT}\right) \tag{9}$$

where R is the gas constant, T is the temperature, and τ_0 is the elementary Rouse timescale. σ is a parameter that portrays the mobility of the associative cross-links within the vitrimer matrix. E_a^{sticky} is defined as

$$\begin{aligned} E_a^{\text{sticky}} &= \frac{\partial}{\partial\left(\frac{1}{RT}\right)} \ln \tau_{\text{XL}} \\ &= \frac{\partial}{\partial\left(\frac{1}{RT}\right)} \ln \sigma + \frac{\partial}{\partial\left(\frac{1}{RT}\right)} \ln \tau_0 + \frac{\partial}{\partial\left(\frac{1}{RT}\right)} \frac{E_a^{\text{sm}}}{RT} \end{aligned} \tag{10}$$

$$E_a^{\text{sticky}} = \frac{\partial}{\partial\left(\frac{1}{RT}\right)} \ln \sigma + E_a^{\text{WLF}} + E_a^{\text{sm}} \tag{11}$$

$$E_a^{\text{WLF}} = \frac{\partial}{\partial\left(\frac{1}{RT}\right)} \ln \tau_0 \tag{12}$$

In our prior work, we assumed that σ was independent of temperature, causing the first derivative term in eq 11 to cancel and resulting in the form of E_a^{sticky} described in eq 1. Relaxing that assumption creates an additional contribution to E_a^{sticky}

$$E_a^{\text{sticky}} = \frac{\partial}{\partial\left(\frac{1}{RT}\right)} \ln \sigma + E_a^{\text{WLF}} + E_a^{\text{sm}} = E_a^{\sigma} + E_a^{\text{WLF}} + E_a^{\text{sm}} \tag{13}$$

For this reason, we speculate that the larger-than-expected values for E_a^{creep} originate from the temperature dependence of σ.

Although we introduced the σ parameter in our previous work,[58] the relationship between cross-link mobility and τ_{XL} has already been studied through the lens of microscopic theories, albeit mostly for networks with *dissociative* cross-links that rearrange via an elimination/addition pathway.[3,69,74] For the Renormalized Bond Lifetime Model (RBLM) of Rubinstein and Semenov, τ_{XL} accounts for both the subdiffusive motions of backbone repeat units and cross-link reassociations that do not contribute to stress relaxation.[69,73] We derive explicit expressions for the cross-link mobility and long-time dynamics activation energy (σ^{RBLM} and E_a^{RBLM}, respectively) using the RBLM framework and assuming the cross-links undergo Rouse-like subdiffusive motion

$$\sigma^{\text{RBLM}} = Z\left(1 + Z^3 \exp\left(-\frac{E_a^{\text{sm}}}{RT}\right)\right) \tag{14}$$

$$E_a^{\text{RBLM}} = E_a^{\text{WLF}} + \frac{E_a^{\text{sm}}}{1 + Z^3 \exp\left(\frac{-E_a^{\text{sm}}}{RT}\right)} \tag{15}$$

where Z is the number of times a cross-linkable group reassociates with an old partner (see the Supporting Information for derivation). Another transient network theory is the model of Ghosh and Schweizer (GS), in which local frictional resistance of the backbone segments attenuates the overall temperature dependence of the network relaxation.[54,80] Combining the RBLM and GS models, we develop alternative forms of the cross-link mobility and long-time dynamics activation energy (σ^{GS} and E_a^{GS})

$$\sigma^{\text{GS}} = Z\left(\left(\frac{\tau_0}{\tau}\right)^{\nu-1} + (1 + Z^3) \exp\left(-\frac{E_a^{\text{sm}}}{RT}\right)\right) \tag{16}$$

$$E_a^{\text{GS}} = E_a^{\text{WLF}} + \frac{\tau_0^{\nu-1}E_a^{\text{sm}} + (\nu - 1)E_a^{\text{WLF}}}{1 + \frac{1+Z^3}{\tau^{1-\nu}\tau_0^{\nu-1} \exp\left(\frac{E_a^{\text{sm}}}{RT}\right)}} \tag{17}$$

where ν is a decoupling exponent and τ is the elementary attempt time for activated relaxation.[80] Figure S29 depicts σ^{RBLM} and σ^{GS} versus T_g.

While eqs 15 and 17 provide elegantly simple forms for the activation energies, they do not accurately describe our experimental data. The second terms in each expression essentially diminish the influence of E_a^{sm}, leading to weaker temperature dependences relative to E_a^{sticky}. Consequently, both E_a^{RBLM} and E_a^{GS} also severely underestimate the measured E_a^{creep}. The use of the Phantom Network N_{XL} values does not change the result (Figure S33). This trend is further demonstrated in Figure 7, which illustrates E_a^{σ} versus T_g (see the Supporting Information for details of calculation). There, the E_a^{σ} values predicted by the RBLM and GS models are negative, contradicting experimental observations.

Based on the analyses performed in Figures 6 and 7, a key point of this work is that RBLM-inspired models—which describe dissociative networks—are destined to be qualitatively

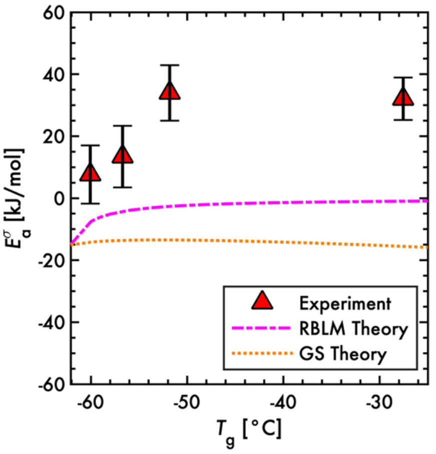

Figure 7. E_a^σ versus T_g: Experimental data is obtained from creep data using $E_a^\sigma = E_a^{creep} - E_a^{WLF} - E_a^{sm}$. Predictions for RBLM and GS theories are obtained by replacing E_a^{creep} in the expression above with E_a^{RBLM} and E_a^{GS} from eqs 15 and 17, respectively.

inconsistent with experiments on associative vitrimer networks. It is worthwhile to point out that this behavior persists even if the RBLM is adapted for associative networks by forcing the number of reassociations $Z = 1$. Thus, the discrepancy between the expected and measured values of E_a^{creep} becomes larger after incorporating the temperature dependence of cross-link mobility as modeled in established theories.

One possible contribution toward this discrepancy stems from assumptions regarding E_a^{sm}. For dioxaborolane metathesis, E_a^{sm} was determined via kinetics studies on small-molecule boronic esters in the bulk (i.e., no solvent present).[15] Use of the sticky Rouse, RBLM, and GS models hinges on the assumption that the E_a^{sm} measured for the small-molecule cross-linker analogues directly translates to the vitrimer system. Furthermore, the GS model—as incorporated in this work—presupposes that the effective association free energy barrier ΔF is equal to E_a^{sm} and neglects any associated change in entropy. The idea that E_a^{sm} measured in small-molecule studies is preserved when these chemical moieties are incorporated into polymer matrices must be further assessed for validity.

■ CONCLUSIONS

The linear viscoelasticity of PB vitrimers with varying dioxaborolane cross-link density was evaluated using a combination of SAOS, creep, and stress relaxation. The short- and long-time dynamics exhibit different temperature dependences, preventing complete superposition of the stress relaxation curves at varying temperatures well above T_g. The activation energy of the short-time dynamics is consistent with the monomer friction of the PB backbone, suggesting that segmental motions precipitate the initial cross-link exchange events. The long-time dynamics, characterized by prolonged power law regimes in stress relaxation and creep measurements, express an activation energy that is larger than the predicted values of the sticky Rouse and sticky reptation models.

We speculate that the discrepancy between the measured E_a^{creep} and predicted E_a^{sticky} values originates from the temperature dependence of the cross-link mobility within the PB backbone matrix, σ. Theories that describe cross-linker subdiffusion, such as the RBLM and GS models, have been successfully used to describe the dynamics of polymer networks with dissociative cross-links. For PB vitrimers with associative cross-links, however, we find that they are unable to resolve the discrepancy between E_a^{creep} and E_a^{sticky}. In fact, modeling cross-linker subdiffusion using these theories exacerbates the disagreement between the measured and theoretical activation energy estimates. The failure of these dissociative network models highlights the need for theories that describe the dynamics of vitrimers with associative cross-links.

Our findings identify knowledge gaps in understanding the role of E_a^{sm} and the mechanism of associative cross-link exchange within a vitrimer system. To resolve these open questions, we propose investigating vitrimer rheology using a framework centered around the role of the cross-link mobility σ. Developing a molecular description of σ for vitrimers will not only clarify the features of the linear viscoelastic response but also the dynamics under larger strains and stresses. Knowledge of the latter regime is of particular importance for optimizing the flow behavior during extrusion, injection, 3D printing, and other standard forms of polymer processing.[24,64,81] Moving forward, the combination of experiment, computations, and theory will be needed to illuminate the impact of molecular structure on vitrimer dynamics.

■ ASSOCIATED CONTENT

Supporting Information

The Supporting Information is available free of charge at https://pubs.acs.org/doi/10.1021/acs.macromol.3c00883.

> Characterization of precursor polybutadiene, ^1H and ^{13}C nuclear magnetic resonance spectroscopy of dioxaborolane cross-linker, PB vitrimer attenuated total reflectance infrared spectroscopy, PB vitrimer thermal characterization, PB vitrimer small-angle X-ray scattering, estimated insoluble fraction for networks with a statistical cross-link distribution, PB vitrimer strain amplitude sweeps, parameters for rheological measurements, preconditioning procedure for rheological measurements, SAOS and creep data for PB-*v*-1, PB-*v*-8, and PB-*v*-15, tan δ data, creep recovery compliance data, a_{SAOS} and a_{creep} shift factors for PB-*v*-1, PB-*v*-8, and PB-*v*-15, plateau moduli and vertical shift factors, stress relaxation for PB-*v*-1, PB-*v*-8, and PB-*v*-15, 24 h creep of PB-*v*-15, static cross-link PB thermoset synthesis and SAOS, creep, and stress relaxation, Prony series analysis for PB-*v*-4, derivation of E_a^{WLF}, σ^{RBLM}, E_a^{RBLM}, σ^{GS}, and E_a^{GS} models, deconvolution of ATIR-IR spectra, isothermal SAOS measurements, glass-transition temperature and activation energy analysis using Phantom Network N_{XL}, and double Arrhenius analysis of a_{SAOS} and a_{creep} (PDF)

■ AUTHOR INFORMATION

Corresponding Authors

Ralm G. Ricarte − *Department of Chemical and Biomedical Engineering, FAMU-FSU College of Engineering, Tallahassee, Florida 32310, United States;* orcid.org/0000-0003-1018-6083; Email: rricarte@eng.famu.fsu.edu

Sachin Shanbhag − *Department of Scientific Computing, Florida State University, Tallahassee, Florida 32306, United States;* orcid.org/0000-0002-7807-112X; Email: sshanbhag@fsu.edu

Authors

Dana Ezzeddine − *Department of Chemical and Biomedical Engineering, FAMU-FSU College of Engineering, Tallahassee, Florida 32310, United States;* orcid.org/0000-0003-1633-3953

Daniel Barzycki − *Department of Chemical and Biomedical Engineering, FAMU-FSU College of Engineering, Tallahassee, Florida 32310, United States*

Kevin Fay − *Department of Chemical and Biomedical Engineering, FAMU-FSU College of Engineering, Tallahassee, Florida 32310, United States*

Complete contact information is available at: https://pubs.acs.org/10.1021/acs.macromol.3c00883

Notes

The authors declare no competing financial interest.

■ ACKNOWLEDGMENTS

The authors are very grateful to Dr. Rufina Alamo and the Alamo Laboratory for use of their differential scanning calorimeter, Dr. Rebekah Sweat and the Sweat Laboratory for use of their rheometer for measurements on the precursor PB, Dr. Subramanian Ramakrishnan and the Ramakrishnan Laboratory for use of their rheometer for conducting preliminary measurements, Dr. Justin Kennemur and the Kennemur Laboratory for use of their size exclusion chromatography instrument, Florida State University High-Performance Materials Institute for use of their characterization equipment, and Florida State University Department of Chemistry and Biochemistry for use of the Nuclear Magnetic Resonance Spectroscopy Facility. The authors thank Dr. Stephanie Marxsen, Guanrui Li, Jaehoon Jang, and Zachary Bauer for help with experiments. This research used resources of the Advanced Photon Source, a U.S. Department of Energy (DOE) Office of Science User Facility operated for the DOE Office of Science by Argonne National Laboratory under Contract DE-AC02-06CH11357. The authors thank Steven Weigand of the Advanced Photon Source for his help in using beamline DND-CAT 5ID-D. This work was supported primarily by the National Science Foundation (DMR-2144007). This work was partially supported by funds provided by the Oak Ridge Associated Universities Foundation, ORAU-Directed Research and Development Program. This work is based in part upon work supported by the National Science Foundation under grant no. NSF DMR-1727870. This work was also supported using start-up funds from Florida State University and the Florida A&M−Florida State University College of Engineering.

■ REFERENCES

(1) Kloxin, C. J.; Bowman, C. N. Covalent Adaptable Networks: Smart, Reconfigurable and Responsive Network Systems. *Chem. Soc. Rev.* **2013**, *42*, 7161−7173.

(2) Scheutz, G. M.; Lessard, J. J.; Sims, M. B.; Sumerlin, B. S. Adaptable Crosslinks in Polymeric Materials: Resolving the Intersection of Thermoplastics and Thermosets. *J. Am. Chem. Soc.* **2019**, *141*, 16181−16196.

(3) Winne, J. M.; Leibler, L.; Prez, F. E. D. Dynamic Covalent Chemistry in Polymer Networks: A Mechanistic Perspective. *Polym. Chem.* **2019**, *10*, 6091−6108.

(4) Van Zee, N. J.; Nicolaÿ, R. Vitrimers: Permanently Crosslinked Polymers with Dynamic Network Topology. *Prog. Polym. Sci.* **2020**, *104*, No. 101233.

(5) Porath, L.; Soman, B.; Jing, B. B.; Evans, C. M. Vitrimers: Using Dynamic Associative Bonds to Control Viscoelasticity, Assembly, and Functionality in Polymer Networks. *ACS Macro Lett.* **2022**, *11*, 475−483.

(6) Green, M. S.; Tobolsky, A. V. A New Approach to the Theory of Relaxing Polymeric Media. *J. Chem. Phys.* **1946**, *14*, 80−92.

(7) Flory, P. J. Elasticity of Polymer Networks Cross-Linked in States of Strain. *Trans. Faraday Soc.* **1960**, *56*, 722−743.

(8) Fricker, H. S. The Effects on Rubber Elasticity of the Addition and Scission of Cross-Links under Strain. *Proc. R. Soc. Lond. A: Math. Phys. Sci.* **1973**, *335*, 267−287.

(9) Fricker, H. S. On the Theory of Stress Relaxation by Cross-Link Reorganization. *Proc. R. Soc. Lond. A: Math. Phys. Sci.* **1973**, *335*, 289−300.

(10) Baxandall, L. G. Dynamics of Reversibly Crosslinked Chains. *Macromolecules* **1989**, *22*, 1982−1988.

(11) Leibler, L.; Rubinstein, M.; Colby, R. H. Dynamics of Reversible Networks. *Macromolecules* **1991**, *24*, 4701−4707.

(12) Leibler, L.; Rubinstein, M.; Colby, R. H. Dynamics of Telechelic Ionomers. Can Polymers Diffuse Large Distances without Relaxing Stress? *J. Phys. II* **1993**, *3*, 1581−1590.

(13) Chabert, E.; Vial, J.; Cauchois, J.-P.; Mihaluta, M.; Tournilhac, F. Multiple Welding of Long Fiber Epoxy Vitrimer Composites. *Soft Matter* **2016**, *12*, 4838−4845.

(14) Imbernon, L.; Norvez, S. From Landfilling to Vitrimer Chemistry in Rubber Life Cycle. *Eur. Polym. J.* **2016**, *82*, 347−376.

(15) Röttger, M.; Domenech, T.; Weegen, R. van. der.; Breuillac, A.; Nicolaÿ, R.; Leibler, L. High-Performance Vitrimers from Commodity Thermoplastics through Dioxaborolane Metathesis. *Science* **2017**, *356*, 62−65.

(16) Demongeot, A.; Groote, R.; Goossens, H.; Hoeks, T.; Tournilhac, F.; Leibler, L. Cross-Linking of Poly(Butylene Terephthalate) by Reactive Extrusion Using Zn(II) Epoxy-Vitrimer Chemistry. *Macromolecules* **2017**, *50*, 6117−6127.

(17) Shi, Q.; Yu, K.; Kuang, X.; Mu, X.; Dunn, C. K.; Dunn, M. L.; Wang, T.; Qi, H. J. Recyclable 3D Printing of Vitrimer Epoxy. *Mater. Horiz.* **2017**, *4*, 598−607.

(18) Jing, B. B.; Evans, C. M. Catalyst-Free Dynamic Networks for Recyclable, Self-Healing Solid Polymer Electrolytes. *J. Am. Chem. Soc.* **2019**, *141*, 18932−18937.

(19) Lee, J.; Jing, B. B.; Porath, L. E.; Sottos, N. R.; Evans, C. M. Shock Wave Energy Dissipation in Catalyst-Free Poly(Dimethylsiloxane) Vitrimers. *Macromolecules* **2020**, *53*, 4741−4747.

(20) Lessard, J. J.; Scheutz, G. M.; Hughes, R. W.; Sumerlin, B. S. Polystyrene-Based Vitrimers: Inexpensive and Recyclable Thermosets. *ACS Appl. Polym. Mater.* **2020**, *2*, 3044−3048.

(21) Lv, G.; Soman, B.; Shan, N.; Evans, C. M.; Cahill, D. G. Effect of Linker Length and Temperature on the Thermal Conductivity of Ethylene Dynamic Networks. *ACS Macro Lett.* **2021**, *10*, 1088−1093.

(22) Ma, J.; Porath, L. E.; Haque, M. F.; Sett, S.; Rabbi, K. F.; Nam, S.; Miljkovic, N.; Evans, C. M. Ultra-Thin Self-Healing Vitrimer Coatings for Durable Hydrophobicity. *Nat. Commun.* **2021**, *12*, No. 5210.

(23) Farge, L.; Hoppe, S.; Daujat, V.; Tournilhac, F.; André, S. Solid Rheological Properties of PBT-Based Vitrimers. *Macromolecules* **2021**, *54*, 1838−1849.

(24) Kim, S.; Rahman, M. A.; Arifuzzaman, M.; Gilmer, D. B.; Li, B.; Wilt, J. K.; Lara-Curzio, E.; Saito, T. Closed-Loop Additive Manufacturing of Upcycled Commodity Plastic through Dynamic Cross-Linking. *Sci. Adv.* **2022**, *8*, No. eabn6006.

(25) Debsharma, T.; Amfilochiou, V.; Wróblewska, A. A.; Baere, I. D.; Paepegem, W. V.; Prez, F. E. D. Fast Dynamic Siloxane Exchange Mechanism for Reshapable Vitrimer Composites. *J. Am. Chem. Soc.* **2022**, *144*, 12280−12289.

(26) Fang, H.; Gao, X.; Zhang, F.; Zhou, W.; Qi, G.; Song, K.; Cheng, S.; Ding, Y.; Winter, H. H. Triblock Elastomeric Vitrimers: Preparation, Morphology, Rheology, and Applications. *Macromolecules* **2022**, *55*, 10900−10911.

(27) Chappuis, S.; Edera, P.; Cloitre, M.; Tournilhac, F. Enriching an Exchangeable Network with One of Its Components: The Key to High-T_g Epoxy Vitrimers with Accelerated Relaxation. *Macromolecules* **2022**, *55*, 6982−6991.

(28) Langenbach, J.; Bakkali-Hassani, C.; Poutrel, Q.-A.; Georgopoulou, A.; Clemens, F.; Tournilhac, F.; Norvez, S. Adhesion and Stiffness Matching in Epoxy-Vitrimers/Strain Sensor Fiber Laminates. *ACS Appl. Polym. Mater.* **2022**, *4*, 1264−1275.

(29) Van Lijsebetten, F.; Engelen, S.; Bauters, E.; Vooren, W. V.; Smulders, M. M. J.; Prez, F. E. D. Recyclable Vitrimer Epoxy Coatings for Durable Protection. *Eur. Polym. J.* **2022**, *176*, No. 111426.

(30) Lv, G.; Li, X.; Jensen, E.; Soman, B.; Tsao, Y.-H.; Evans, C. M.; Cahill, D. G. Dynamic Covalent Bonds in Vitrimers Enable 1.0 W/(m K) Intrinsic Thermal Conductivity. *Macromolecules* **2023**, *56*, 1554−1561.

(31) Fabrizio, L.; Arrigo, R.; Scrivani, M. T.; Monti, M.; Fina, A. Upcycling of PET from Recycled Food Packaging Trays via Vitrimers Chemistry. *Polymer* **2023**, *266*, No. 125618.

(32) Bakkali-Hassani, C.; Edera, P.; Langenbach, J.; Poutrel, Q.-A.; Norvez, S.; Gresil, M.; Tournilhac, F. Epoxy Vitrimer Materials by Lipase-Catalyzed Network Formation and Exchange Reactions. *ACS Macro Lett.* **2023**, *12*, 338−343.

(33) Stewart, K. A.; DeLellis, D. P.; Lessard, J. J.; Rynk, J. F.; Sumerlin, B. S. Dynamic Ablative Networks: Shapeable Heat-Shielding Materials. *ACS Appl. Mater. Interfaces* **2023**, *15*, 25212−25223.

(34) Montarnal, D.; Capelot, M.; Tournilhac, F.; Leibler, L. Silica-Like Malleable Materials from Permanent Organic Networks. *Science* **2011**, *334*, 965−968.

(35) Capelot, M.; Unterlass, M. M.; Tournilhac, F.; Leibler, L. Catalytic Control of the Vitrimer Glass Transition. *ACS Macro Lett.* **2012**, *1*, 789−792.

(36) Capelot, M.; Montarnal, D.; Tournilhac, F.; Leibler, L. Metal-Catalyzed Transesterification for Healing and Assembling of Thermosets. *J. Am. Chem. Soc.* **2012**, *134*, 7664−7667.

(37) Nishimura, Y.; Chung, J.; Muradyan, H.; Guan, Z. Silyl Ether as a Robust and Thermally Stable Dynamic Covalent Motif for Malleable Polymer Design. *J. Am. Chem. Soc.* **2017**, *139*, 14881−14884.

(38) Lessard, J. J.; Garcia, L. F.; Easterling, C. P.; Sims, M. B.; Bentz, K. C.; Arencibia, S.; Savin, D. A.; Sumerlin, B. S. Catalyst-Free Vitrimers from Vinyl Polymers. *Macromolecules* **2019**, *52*, 2105−2111.

(39) Spiesschaert, Y.; Taplan, C.; Stricker, L.; Guerre, M.; Winne, J. M.; Prez, F. E. D. Influence of the Polymer Matrix on the Viscoelastic Behaviour of Vitrimers. *Polym. Chem.* **2020**, *11*, 5377−5385.

(40) Hajj, R.; Duval, A.; Dhers, S.; Avérous, L. Network Design to Control Polyimine Vitrimer Properties: Physical Versus Chemical Approach. *Macromolecules* **2020**, *53*, 3796−3805.

(41) Meng, F.; Pritchard, R. H.; Terentjev, E. M. Stress Relaxation, Dynamics, and Plasticity of Transient Polymer Networks. *Macromolecules* **2016**, *49*, 2843−2852.

(42) Li, L.; Chen, X.; Jin, K.; Torkelson, J. M. Vitrimers Designed Both To Strongly Suppress Creep and To Recover Original Cross-Link Density after Reprocessing: Quantitative Theory and Experiments. *Macromolecules* **2018**, *51*, 5537−5546.

(43) Meng, F.; Saed, M. O.; Terentjev, E. M. Elasticity and Relaxation in Full and Partial Vitrimer Networks. *Macromolecules* **2019**, *52*, 7423−7429.

(44) El-Zaatari, B. M.; Ishibashi, J. S. A.; Kalow, J. A. Cross-Linker Control of Vitrimer Flow. *Polym. Chem.* **2020**, *11*, 5339−5345.

(45) Saed, M. O.; Gablier, A.; Terentejv, E. M. Liquid Crystalline Vitrimers with Full or Partial Boronic-Ester Bond Exchange. *Adv. Funct. Mater.* **2020**, *30*, No. 1906458.

(46) Song, Z.; Wang, Z.; Cai, S. Mechanics of Vitrimer with Hybrid Networks. *Mech. Mater.* **2021**, *153*, No. 103687.

(47) Anaya, O.; Jourdain, A.; Antoniuk, I.; Romdhane, H. B.; Montarnal, D.; Drockenmuller, E. Tuning the Viscosity Profiles of High-T_g Poly(1,2,3-Triazolium) Covalent Adaptable Networks by the Chemical Structure of the N-Substituents. *Macromolecules* **2021**, *54*, 3281−3292.

(48) Porath, L. E.; Evans, C. M. Importance of Broad Temperature Windows and Multiple Rheological Approaches for Probing Viscoelasticity and Entropic Elasticity in Vitrimers. *Macromolecules* **2021**, *54*, 4782−4791.

(49) Porath, L.; Huang, J.; Ramlawi, N.; Derkaloustian, M.; Ewoldt, R. H.; Evans, C. M. Relaxation of Vitrimers with Kinetically Distinct Mixed Dynamic Bonds. *Macromolecules* **2022**, *55*, 4450−4458.

(50) Xu, H.; Wang, H.; Zhang, Y.; Wu, J. Vinylogous Urethane Based Epoxy Vitrimers with Closed-Loop and Multiple Recycling Routes. *Ind. Eng. Chem. Res.* **2022**, *61*, 17524−17533.

(51) Guerre, M.; Taplan, C.; Nicolaÿ, R.; Winne, J. M.; Prez, F. E. D. Fluorinated Vitrimer Elastomers with a Dual Temperature Response. *J. Am. Chem. Soc.* **2018**, *140*, 13272−13284.

(52) Meng, F.; Saed, M. O.; Terentjev, E. M. Rheology of Vitrimers. *Nat. Commun.* **2022**, *13*, No. 5753.

(53) Perego, A.; Lazarenko, D.; Cloitre, M.; Khabaz, F. Microscopic Dynamics and Viscoelasticity of Vitrimers. *Macromolecules* **2022**, *55*, 7605−7613.

(54) Soman, B.; Schweizer, K. S.; Evans, C. M. Fragile Glass Formation and Non-Arrhenius Upturns in Ethylene Vitrimers Revealed by Dielectric Spectroscopy. *Macromolecules* **2023**, *56*, 166−176.

(55) Jourdain, A.; Asbai, R.; Anaya, O.; Chehimi, M. M.; Drockenmuller, E.; Montarnal, D. Rheological Properties of Covalent Adaptable Networks with 1,2,3-Triazolium Cross-Links: The Missing Link between Vitrimers and Dissociative Networks. *Macromolecules* **2020**, *53*, 1884−1900.

(56) Wu, S.; Yang, H.; Huang, S.; Chen, Q. Relationship between Reaction Kinetics and Chain Dynamics of Vitrimers Based on Dioxaborolane Metathesis. *Macromolecules* **2020**, *53*, 1180−1190.

(57) Wu, S.; Yang, H.; Xu, W.-S.; Chen, Q. Thermodynamics and Reaction Kinetics of Symmetric Vitrimers Based on Dioxaborolane Metathesis. *Macromolecules* **2021**, *54*, 6799−6809.

(58) Ricarte, R. G.; Shanbhag, S. Unentangled Vitrimer Melts: Interplay between Chain Relaxation and Cross-Link Exchange Controls Linear Rheology. *Macromolecules* **2021**, *54*, 3304−3320.

(59) Huang, S.; Han, L.; Ma, H.; Lei, L.; Zhang, R.; Shen, H.; Yang, L.; Li, C.; Zhang, S.; Li, Y. Determination of Refractive Index Increment of Synthetic Polybutadienes and Microstructural Control of Grafting Density and Liquid Crystalline Properties. *Polym. Chem.* **2020**, *11*, 2559−2567.

(60) Breuillac, A.; Kassalias, A.; Nicolaÿ, R. Polybutadiene Vitrimers Based on Dioxaborolane Chemistry and Dual Networks with Static and Dynamic Cross-Links. *Macromolecules* **2019**, *52*, 7102−7113.

(61) David, R. L. A.; Kornfield, J. A. Facile, Efficient Routes to Diverse Protected Thiols and to Their Deprotection and Addition to Create Functional Polymers by Thiol−Ene Coupling. *Macromolecules* **2008**, *41*, 1151−1161.

(62) Ferry, J. *Viscoelastic Properties of Polymers*, 3rd ed.; John Wiley & Sons Inc., 1980.

(63) Ewoldt, R. H.; McKinley, G. H. Creep Ringing in Rheometry or How to Deal with Oft-Discarded Data in Step Stress Tests! *Rheol. Bull.* **2007**, *76*, No. 4.

(64) Ricarte, R. G.; Tournilhac, F.; Cloître, M.; Leibler, L. Linear Viscoelasticity and Flow of Self-Assembled Vitrimers: The Case of a Polyethylene/Dioxaborolane System. *Macromolecules* **2020**, *53*, 1852−1866.

(65) de Gennes, P. G. Kinetics of Diffusion-controlled Processes in Dense Polymer Systems. I. Nonentangled Regimes. *J. Chem. Phys.* **1982**, *76*, 3316−3321.

(66) de Gennes, P. G. Kinetics of Diffusion-controlled Processes in Dense Polymer Systems. II. Effects of Entanglements. *J. Chem. Phys.* **1982**, *76*, 3322−3326.

(67) Friedman, B.; O'Shaughnessy, B. Kinetics of Intermolecular Reactions in Dilute Polymer Solutions and Unentangled Melts. *Macromolecules* **1993**, *26*, 5726−5739.

(68) Semenov, A. N.; Rubinstein, M. Thermoreversible Gelation in Solutions of Associative Polymers. 1. Statics. *Macromolecules* **1998**, *31*, 1373−1385.

(69) Rubinstein, M.; Semenov, A. N. Thermoreversible Gelation in Solutions of Associating Polymers. 2. Linear Dynamics. *Macromolecules* **1998**, *31*, 1386−1397.

(70) Semenov, A. N.; Rubinstein, M. Dynamics of Strongly Entangled Polymer Systems: Activated Reptation. *Eur. Phys. J. B* **1998**, *1*, 87−94.

(71) Rubinstein, M.; Semenov, A. N. Dynamics of Entangled Solutions of Associating Polymers. *Macromolecules* **2001**, *34*, 1058−1068.

(72) Semenov, A. N.; Rubinstein, M. Dynamics of Entangled Associating Polymers with Large Aggregates. *Macromolecules* **2002**, *35*, 4821−4837.

(73) Stukalin, E. B.; Cai, L.-H.; Kumar, N. A.; Leibler, L.; Rubinstein, M. Self-Healing of Unentangled Polymer Networks with Reversible Bonds. *Macromolecules* **2013**, *46*, 7525−7541.

(74) Shanbhag, S.; Ricarte, R. G. On the Effective Lifetime of Reversible Bonds in Transient Networks. *Macromol. Theory Simul.* **2023**, *32*, No. 2300002.

(75) Chen, Q.; Colby, R. H. Linear Viscoelasticity of Sulfonated Styrene Oligomers near the Sol-Gel Transition. *Korea−Aust. Rheol. J.* **2014**, *26*, 257−261.

(76) Zhang, Z.; Chen, Q.; Colby, R. H. Dynamics of Associative Polymers. *Soft Matter* **2018**, *14*, 2961−2977.

(77) Chen, Q. Dynamics in Miscible Polymer Blends and Associative Polymers. *Nihon Reoroji Gakkaishi* **2019**, *47*, 197−205.

(78) Yang, H.; Wu, S.; Chen, Q. Linear Viscoelasticity of Double Associative Polymers with Varied Density of the Secondary Interaction. *J. Rheol.* **2022**, *66*, 1113−1123.

(79) Wu, S.; Chen, Q. Advances and New Opportunities in the Rheology of Physically and Chemically Reversible Polymers. *Macromolecules* **2022**, *55*, 697−714.

(80) Ghosh, A.; Schweizer, K. S. Physical Bond Breaking in Associating Copolymer Liquids. *ACS Macro Lett.* **2021**, *10*, 122−128.

(81) Ricarte, R. G.; Tournilhac, F.; Leibler, L. Phase Separation and Self-Assembly in Vitrimers: Hierarchical Morphology of Molten and Semicrystalline Polyethylene/Dioxaborolane Maleimide Systems. *Macromolecules* **2019**, *52*, 432−443.

https://doi.org/10.1021/acs.macromol.3c00883